
PERGAMON

Journal of the Mechanics and Physics of Solids
50 (2002) 549–569

JOURNAL OF THE
MECHANICS AND
PHYSICS OF SOLIDS

www.elsevier.com/locate/jmps

Potential flow model of cavitation-induced interfacial fracture in a confined ductile layer

Sulin Zhang[a], K. Jimmy Hsia[a,b,*], Arne J. Pearlstein[b,c]

[a] *Department of Theoretical and Applied Mechanics, University of Illinois at Urbana-Champaign, 104 South Wright Street, Urbana, IL 61801, USA*
[b] *Frederick Seitz Materials Research Laboratory, University of Illinois at Urbana-Champaign, 104 South Goodwin Avenue, Urbana, IL 61801, USA*
[c] *Department of Mechanical and Industrial Engineering, University of Illinois at Urbana-Champaign, 1206 West Green Street, Urbana, IL 61801, USA*

Received 14 November 2000; received in revised form 8 May 2001; accepted 8 May 2001

Abstract

Fracture of a thin ductile layer sandwiched between stiff substrates often results from growth and coalescence of microscopic cavities ahead of an extending crack. Cavitation induced by plastic flow in a confined, ductile layer is analyzed here to evaluate the interfacial fracture toughness of such sandwich structures. For rigid–plastic materials, a new method is proposed in which the potential flow field of a fluid is used to approximate the plastic deformation. The principle of virtual work rate is applied to determine the equivalent traction–separation law. The method is demonstrated and validated for spherically symmetric cavity growth, for which an exact solution exists. We then study in detail the growth of an initially spherical cavity in a cylindrical bar of finite length subject to uniform traction at its ends. The results show that the stress–separation curves depend strongly on initial cavity size and the strain-hardening exponent, and weakly on the nominal strain. The method has clear advantages over numerical methods, such as finite-element analysis, for parametric study of cavity growth with large plastic deformation.

Keywords: A. Cavity growth; A. Fracture toughness; A. Interfacial fracture; B. Ideally plastic material

* Corresponding author. Department of Theoretical and Applied Mechanics, University of Illinois at Urbana-Champaign, 216 Talbot Laboratory, 104 South Wright Street, Urbana, IL 61801, USA. Tel.: +1-217-333-2321; fax: +1-217-244-5707.
E-mail address: kj-hsia@uiuc.edu (K.J. Hsia).

0022-5096/02/$ - see front matter
PII: S0022-5096(01)00089-8

1. Introduction

The strength and durability of sandwich structures consisting of two stiff substrates bonded by a thin adhesive layer are determined by various failure mechanisms, such as interfacial debonding, and cavity nucleation, growth, and coalescence within the adhesive layer. The relative importance of these failure mechanisms is ultimately determined by the interfacial microstructure of the sandwich structure. The present work is motivated by the capability to tailor interfacial microstructures to improve the mechanical properties of adhesively bonded joints (Gao et al., 1999).

Extensive work on failure of ductile layers sandwiched between two stiff substrates shows that high triaxial stresses are developed in the ductile layer due to the constraining effect of the stiff substrates on plastic flow (Ashby et al., 1989; Evans and Dalgleish, 1992). These stresses lead to interfacial debonding or cavity nucleation ahead of the crack tip. When the interface is relatively strong, interfacial failure occurs by growth and coalescence of microscopic cavities ahead of an extending crack. For this failure mechanism, cavities nucleate either from the interface or within the interfacial layer (Mao and Evans, 1997), as shown schematically in Fig. 1. Cavity nucleation usually occurs at the sites of initial defects on the interface, such as surface pores in aluminum oxide films (cf. Clearfield et al., 1990) or at second-phase inclusions within the ductile layer. Therefore, the initial density of cavities is determined by either the morphological features of the interface or the distribution of impurities in the ductile layer.

A material's resistance to fracture can be characterized by its stress–separation curve—the relation between local stress at a material point and atomic separation. When cavitation occurs ahead of the crack tip, an equivalent stress–separation curve can be used to estimate the fracture toughness, as demonstrated by Tvergaard and Hutchinson (1992, 1996) for materials undergoing plastic deformation. The equivalent stress–separation curve can be obtained by averaging microscopic stress and displacement over a volume large compared to the local cavity size but small compared to the characteristic length scale, e.g., the layer thickness. In Tvergaard and Hutchinson's analyses, the stress–separation law was approximated by simple functions not derived from microscopic mechanisms. On the other hand, most studies of the stress–separation law for cavity growth make use of the finite-element method, which is computationally

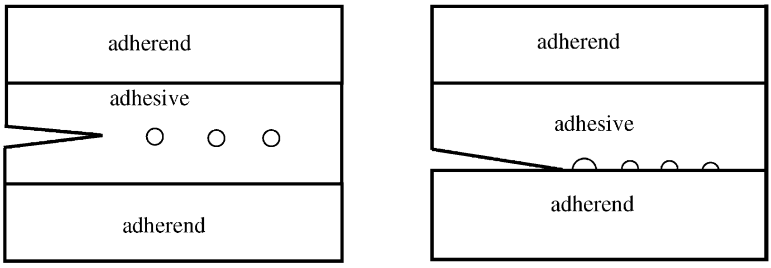

Fig. 1. Schematic of the fracture mechanism: crack propagates by cavity nucleation, growth and coalescence. (a) Cavity nucleates within the interface layer. (b) Cavity nucleates along the interface.

intensive. Without remeshing at each stage, finite-element approaches are limited to incomplete stress–separation curves (Tvergaard, 1997).

In this work we determine the full stress–separation relation due to cavitation induced by plastic flow. We extend the two-dimensional potential-flow approach developed by Zhang and Hsia (2001) to the axisymmetric case of cavity growth in a finite cylinder. The principle of virtual work rate is employed to derive stress–separation relations. A spherically symmetric cavity growth problem, for which a closed-form solution exists, is used to demonstrate and validate the method. The method is then used to obtain full stress–separation curves for growth of a cavity centered in a cylindrical bar. The results show that the stress–separation curves depend not only on the material constants, but also on interfacial microstructure.

2. Governing equations of a rigid–plastic material

Consider an internal cavity in a perfectly plastic or strain-hardening rigid–plastic incompressible material. A uniaxial relation between the true stress, σ, and the logarithmic strain, ε, of the solid is given by

$$\sigma/\sigma_{\mathrm{Y}} = f(\varepsilon) \equiv |\varepsilon/\varepsilon_{\mathrm{Y}}|^{N} \operatorname{sign}(\varepsilon), \tag{1}$$

where σ_{Y} is the tensile yield strength, ε_{Y} is a nominal strain, N is the strain-hardening exponent ($0 \leqslant N < 1$), and $\operatorname{sign}(\varepsilon)$ denotes the sign of ε. The limit $N = 0$ corresponds to a rigid–perfectly plastic material.

We seek to determine a full stress–separation relation for cavity-containing materials subject to specified stress or strain-rate distributions on the boundary. For problems involving nonlinear effects such as large deformation and plasticity, closed-form solutions for the exact velocity field are usually not obtainable, except in one-dimensional cases. Fortunately, a good approximation to the velocity field should be sufficient to establish an accurate stress–displacement relation by making use of the principle of virtual work rate. The incompressibility of the material throughout its deformation history suggests that a good candidate for the approximation is a potential flow generated by a point source and satisfying the same boundary conditions (Lamb, 1932). The potential flow due to a point source at $\boldsymbol{x}_0$ can be determined by solving the boundary-value problem

$$\nabla^2 \phi = Q\delta(\boldsymbol{x} - \boldsymbol{x}_0) \quad \text{in } V, \tag{2a}$$

$$\boldsymbol{n} \cdot \nabla\phi = \boldsymbol{n} \cdot \dot{\boldsymbol{u}}^{s} \quad \text{on } S, \tag{2b}$$

where ϕ is the velocity potential, and V the volume bounded by the cavity and outer surface S of the solid. Here, $\dot{\boldsymbol{u}}^{s}$ is a specified boundary velocity vector, $\boldsymbol{n}$ the unit outward normal to the boundary, $\boldsymbol{x}$ the observation point, Q the strength of the point source and δ the Dirac delta function. By applying the principle of virtual work rate, one has

$$\int_S T_i \dot{u}_i^{s} \,\mathrm{d}S = \int_V \sigma_{ij}\dot{\varepsilon}_{ij} \,\mathrm{d}V, \tag{3}$$

where T_i is the applied traction on the boundary corresponding to $\dot{u}_i^s$, σ_{ij} is the true stress, and $\dot{\varepsilon}_{ij}$ is the true strain rate corresponding to the velocity field associated with the potential flow. We assume that the material obeys the $J-2$ flow rule

$$s_{ij} = \frac{2}{3}\frac{\sigma_e}{\dot{\varepsilon}_e}\dot{\varepsilon}_{ij}, \tag{4}$$

where $s_{ij} = \sigma_{ij} - (\sigma_{kk}/3)\delta_{ij}$ is the deviatoric stress, $\sigma_e = \sqrt{3 s_{ij} s_{ij}/2}$ is the equivalent stress, and $\dot{\varepsilon}_e = \sqrt{2\dot{\varepsilon}_{ij}\dot{\varepsilon}_{ij}/3}$ is the equivalent strain rate. Substituting Eq. (4) into Eq. (3), one has

$$\int_S T_i \dot{u}_i^s \, \mathrm{d}S = \sigma_Y \int_V f(\varepsilon_e)\dot{\varepsilon}_e \, \mathrm{d}V. \tag{5}$$

A nonuniform stress distribution on the boundary can be decomposed into an average stress on the boundary and a perturbation at each point. Thus, Eq. (5) can be rewritten as

$$\frac{\sigma_s}{\sigma_Y} = \frac{\int_V f(\varepsilon_e)\dot{\varepsilon}_e \, \mathrm{d}V - \int_S (\Delta T_i/\sigma_Y)\dot{u}_i^s \, \mathrm{d}S}{\int_S n_i \dot{u}_i^s \, \mathrm{d}S}, \tag{6}$$

where σ_s is the average stress on the boundary and ΔT_i is the perturbation. Eqs. (5) and (6) pertain to the current, deformed configuration. For simple configurations, the integrals in Eqs. (5) and (6) can be transformed from the current to the initial configuration analytically, which facilitates numerical evaluation, as shown in Section 3 for a sphere. Analytical transformation is not possible for complicated configurations, for which we evaluate the stress–separation curves by the accumulated Lagrangian method (McMeeking and Rice, 1975) based on an Eulerian formulation (see Section 4).

3. Cavity growth in a sphere

As a first application of the procedure described in the previous section, we consider a spherical cavity of initial radius R_0 centered in an isotropic, rigid–plastic spherical body of initial radius R_1 subject to a hydrostatic tension σ_s on the outer boundary (see Fig. 2). An intuitive approximation to the plastic deformation field in the sphere is the potential flow due to a point source of strength Q at the origin, given by

$$\phi = -\frac{Q}{4\pi r}, \tag{7}$$

where r denotes the distance from the center of the sphere in the deformed configuration. The only nonzero velocity component associated with the potential flow is $\dot{u}_r = Q/4\pi r^2$, from which the strain rate components can be obtained as

$$\dot{\varepsilon}_e = -\dot{\varepsilon}_r = 2\dot{\varepsilon}_\theta = 2\dot{\varepsilon}_\varphi = Q/2\pi r^3. \tag{8}$$

Integrating $\dot{u}_r$ with respect to time, subject to the initial condition $r|_{t=0} = R$, gives

$$Qt = \frac{4\pi}{3}(r^3 - R^3), \tag{9}$$

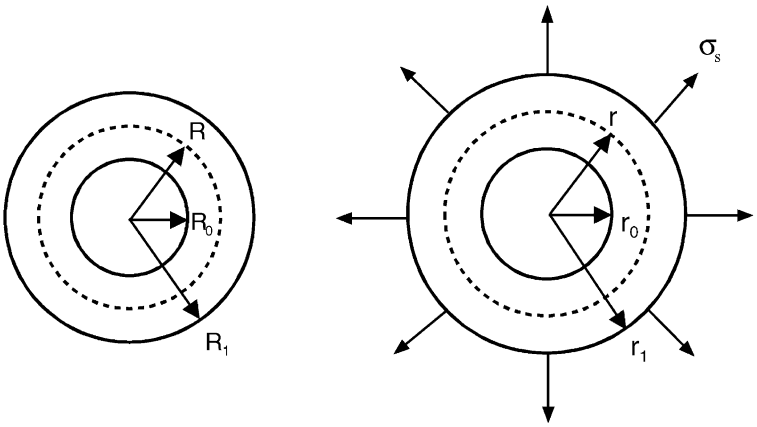

Fig. 2. Geometry of spherically symmetric cavity growth. (a) Initial state. (b) Deformed state.

where R is the distance of a material point from the center of the sphere in the initial configuration. This equation shows that at any instant t, $r^3 - R^3$ is an invariant throughout the body, consistent with the incompressibility of the material. The source strength Q can be interpreted as the changing rate of cavity volume, and is related to the initial cavity radius R_0 by

$$Q = 4\pi R_0^2 \dot{R}_0. \tag{10}$$

Substituting Eq. (8) into Eq. (6) and noting that for the spherically symmetrical case $\Delta T_i = 0$, one obtains

$$\frac{\sigma_s}{\sigma_Y} = \frac{1}{2\pi} \int_V f(\varepsilon_e)/2\pi r^3 \, dV. \tag{11}$$

The integral is evaluated in the current domain V. Using the incompressibility result, Eq. (9), one can transform Eq. (11) into the initial (undeformed) configuration, obtaining

$$\frac{\sigma_s(r_0)}{\sigma_Y} = -2 \int_{R_0}^{R_1} \frac{\zeta^2}{\zeta^3 + r_0^3 - R_0^3} f\{\ln[\zeta^2(\zeta^3 + r_0^3 - R_0^3)^{-2/3}]\} \, d\zeta, \tag{12}$$

where r_0 is the radius of the cavity in the deformed state. This solution is identical to the one obtained using classical continuum plasticity theory (Huang et al., 1991), showing the validity of the method.

Stress–separation curves calculated by direct integration of Eq. (12) are shown in Fig. 3. Results obtained by the accumulated Lagrangian method are graphically indistinguishable from those found by direct integration of Eq. (12). The figure shows that the normalized stress reaches its peak at rather early stages of cavity growth, and then decays monotonically. Should the loading process be stress-controlled, reaching the peak stress would correspond to the occurrence of cavitation instability (Ashby et al., 1989; Huang et al., 1991; Hou and Abeyaratne, 1992; Tvergaard and Hutchinson, 1993). The maximum separation stress increases as the strain-hardening exponent increases and decreases as the initial cavity size increases.

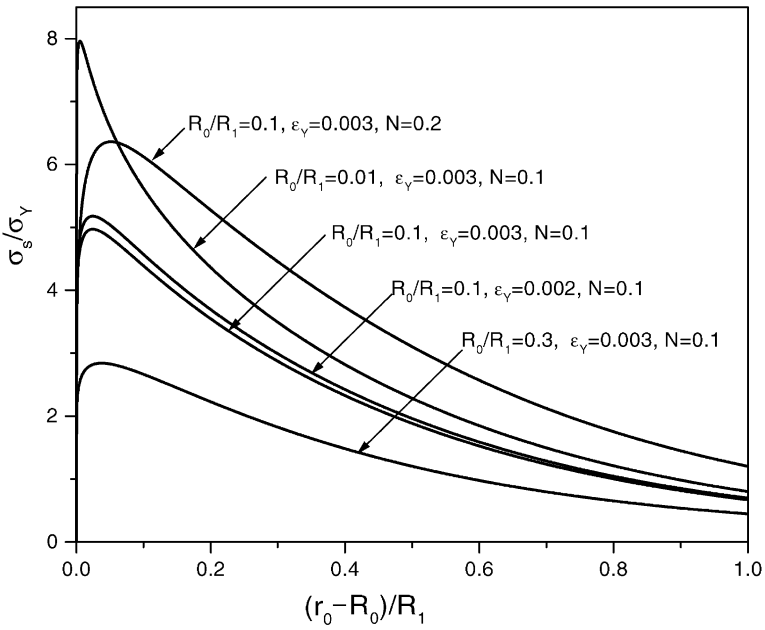

Fig. 3. Stress–separation relations for spherically symmetric case.

4. Cavity growth in a cylindrical bar

In this section, a situation more relevant to cavitation in an adhesive layer is analyzed by the technique developed in Section 2. We consider growth of a cavity of initial radius R_0 centered in a cylindrical bar of radius R and length $2H$ subject to uniform tension at the ends, as shown in Fig. 4. We use Neumann boundary conditions on the cylindrical wall (i.e., the ρ-component of the velocity vanishes at the cylindrical wall) to approximate periodic boundary conditions between adjacent cavities. Unlike the spherically symmetric cavitation problem discussed in Section 3, for which our technique gives the exact solution, the solution for this case is only approximate.

The finite size of the cylindrical bar complicates determination of an approximate potential flow. Rather than solving the boundary-value problem for a finite body, we consider the potential ϕ due to a point source of strength Q at the origin of a cylindrical bar of infinite length. The source strength Q and initial cavity radius R_0 are again related by Eq. (10). In cylindrical coordinates, the potential ϕ is axisymmetric and satisfies a Poisson equation

$$\nabla^2\phi(\boldsymbol{x}) = Q\delta(\boldsymbol{x}) = \frac{Q}{\rho}\delta(\rho)\delta(z), \tag{13}$$

with a singularity at the origin, where $\boldsymbol{x} = (\rho, z)$ are axisymmetric cylindrical coordinates. The boundary condition for the potential can be written as

$$\frac{\partial\phi(\rho,z)}{\partial\rho} = 0 \quad \text{at } \rho = R. \tag{14a}$$

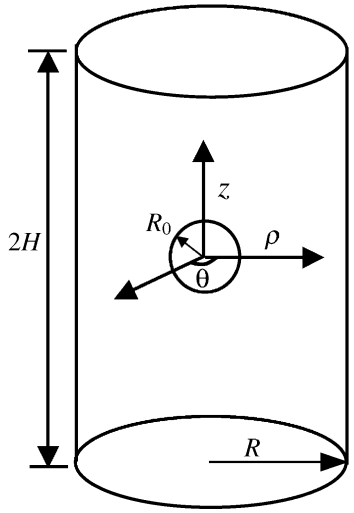

Fig. 4. Geometry of axisymmetric cavity growth.

As z approaches infinity, the boundary conditions on the potential ϕ, compatible [1] with the differential equation and Neumann boundary condition on the cylinder wall, are

$$\frac{\partial\phi(\rho,z)}{\partial z} = \pm\frac{Q}{2\pi R^2} \quad (z \to \pm\infty). \tag{14b}$$

Expanding the solution of Eq. (13) in terms of a complete set of orthogonal radial functions satisfying the boundary condition Eq. (14a), one can use standard techniques (Berg and McGregor, 1966) to find the solution

$$\phi(\boldsymbol{x}) = \frac{Q}{2\pi R}\left[\frac{z}{R} - \sum_{n=1}^{\infty}\frac{J_0(\alpha_n\rho/R)}{\alpha_n J_0^2(\alpha_n)}\mathrm{e}^{-\alpha_n z/R}\right], \tag{15}$$

where J_0 is the zeroth-order Bessel function of the first kind, and α_n is the n-th zero of J_1. The first term on the right-hand side of Eq. (15) corresponds to $\alpha_0 = 0$, and we have omitted an additive constant, which vanishes when ϕ is differentiated.

Unfortunately, the series in Eq. (15) converges slowly as $z/R \to 0$, with the number of required terms increasing inversely with $|z/R|$. Thus, we seek an alternative representation in terms of a Fourier integral outlined in the Appendix A.

Applying the general solution in Eq. (A.13) to the particular case by letting $z' = 0$, one has

$$\phi(\boldsymbol{x}) = -\frac{Q}{2\pi^2}\int_0^{\infty}\cos(kz)\left[\frac{K_1(kR)}{I_1(kR)}I_0(k\rho) + K_0(k\rho)\right]\mathrm{d}k. \tag{16}$$

[1] Compatibility here refers to boundary conditions consistent with Gauss's theorem applied to the potential ϕ in the cylinder and on its surface.

Making use of the integral relation

$$\frac{1}{\sqrt{\rho^2+z^2}} = \frac{2}{\pi}\int_0^\infty \cos(kz)K_0(k\rho)\,\mathrm{d}k, \tag{17}$$

Eq. (16) can be rewritten as

$$\phi(\rho,z) = -\frac{Q}{4\pi\sqrt{\rho^2+z^2}} - \frac{Q}{2\pi^2}\int_0^\infty \cos(kz)\frac{K_1(kR)}{I_1(kR)}I_0(k\rho)\,\mathrm{d}k. \tag{18}$$

The first term on the right-hand side of Eq. (18) represents the potential due to a point source in an unbounded domain, while the second term accounts for boundary effects.

In what follows, we use Eq. (15) to calculate the velocity and strain rates for $|z/R| > \lambda$ (where the choice of λ is discussed below), terminating the series when the relative difference between successively evaluated values of the velocity and strain rates is less than 10^{-5}. The Fourier integral representation in Eq. (18) is used for $|z/R| \leqslant \lambda$.

The velocity field is obtained by taking derivatives of Eq. (18) to get

$$\dot{u}_\rho = \frac{Q\rho}{4\pi r^3} - \frac{Q}{2\pi^2}\int_0^\infty k\cos(kz)\frac{K_1(kR)}{I_1(kR)}I_1(k\rho)\,\mathrm{d}k, \tag{19a}$$

$$\dot{u}_z = \frac{Qz}{4\pi r^3} + \frac{Q}{2\pi^2}\int_0^\infty k\sin(kz)\frac{K_1(kR)}{I_1(kR)}I_0(k\rho)\,\mathrm{d}k, \tag{19b}$$

for $|z/R| \leqslant \lambda$, and of Eq. (15) to get

$$\dot{u}_\rho = \frac{Q}{2\pi R^2}\sum_{n=1}^\infty \frac{J_1(\alpha_n\rho/R)}{J_0^2(\alpha_n)}\mathrm{e}^{-\alpha_n z/R}, \tag{20a}$$

$$\dot{u}_z = \frac{Q}{2\pi R^2}\left[1 + \sum_{n=1}^\infty \frac{J_0(\alpha_n\rho/R)}{J_0^2(\alpha_n)}\mathrm{e}^{-\alpha_n z/R}\right], \tag{20b}$$

for $|z/R| > \lambda$, where $r = \sqrt{\rho^2+z^2}$.

Note that in Eqs. (15) and (18), the potential represents the flow in a cylinder of infinite length. The appropriateness of using this potential flow to approximate the plastic deformation of the finite body should be examined. Fig. 5 shows the radial variation of the normal velocity $\dot{u}_z$ at $z = \pm H$ for different values of the aspect ratio H/R. Here $\dot{u}_z$ is normalized by the normal velocity at $z = \pm H$, $\rho = 0$, denoted by $\dot{u}_0$ in Fig. 5. For $H/R = 1$, the maximum difference in $\dot{u}_z$ across the cross section is about 20%. When the aspect ratio is 2, the maximum difference in $\dot{u}_z$ is only about 1%, and the flow is nearly uniform.

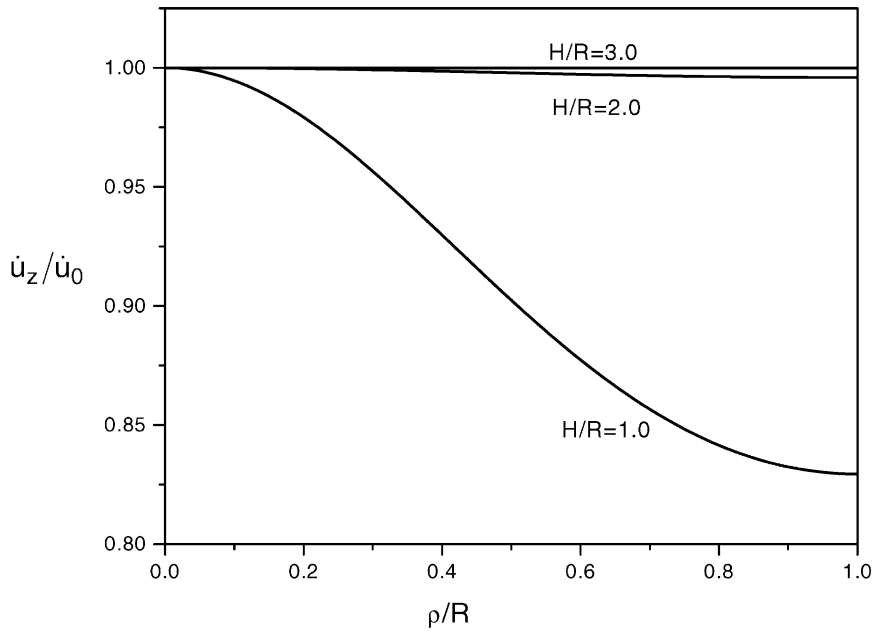

Fig. 5. Uniformity of the velocity field at the interfaces $z = \pm H$.

The Cauchy strain rates associated with this flow field are given by

$$\dot{\varepsilon}_{zz} = \frac{Q}{4\pi}\left(\frac{1}{r^3} - \frac{3z^2}{r^5}\right) + \frac{Q}{2\pi^2}\int_0^\infty k^2 \cos(kz)\frac{K_1(kR)}{I_1(kR)} I_0(k\rho)\,\mathrm{d}k, \tag{21a}$$

$$\dot{\varepsilon}_{\theta\theta} = \frac{Q}{4\pi r^3} - \frac{Q}{2\pi^2\rho}\int_0^\infty k \cos(kz)\frac{K_1(kR)}{I_1(kR)} I_1(k\rho)\,\mathrm{d}k, \tag{21b}$$

$$\dot{\varepsilon}_{\rho z} = -\frac{3Q\rho z}{4\pi r^5} + \frac{Q}{2\pi^2}\int_0^\infty k^2 \sin(kz)\frac{K_1(kR)}{I_1(kR)} I_1(k\rho)\,\mathrm{d}k, \tag{21c}$$

for $|z/R| \leqslant \lambda$, and

$$\dot{\varepsilon}_{zz} = -\frac{Q}{2\pi R^3}\sum_{n=1}^{\infty} \alpha_n \frac{J_0(\alpha_n\rho/R)}{J_0^2(\alpha_n)} \mathrm{e}^{-\alpha_n z/R}, \tag{22a}$$

$$\dot{\varepsilon}_{\theta\theta} = \frac{Q}{2\pi R^2\rho}\sum_{n=1}^{\infty} \frac{J_1(\alpha_n\rho/R)}{J_0^2(\alpha_n)} \mathrm{e}^{-\alpha_n z/R}, \tag{22b}$$

$$\dot{\varepsilon}_{\rho z} = -\frac{Q}{2\pi R^3}\sum_{n=1}^{\infty} \alpha_n \frac{J_1(\alpha_n\rho/R)}{J_0^2(\alpha_n)} \mathrm{e}^{-\alpha_n z/R}, \tag{22c}$$

for $|z/R| > \lambda$, and

$$\dot{\varepsilon}_{\rho\rho} = -(\dot{\varepsilon}_{\theta\theta} + \dot{\varepsilon}_{zz}), \tag{23a}$$

$$\dot{\varepsilon}_{\rho\theta} = 0, \tag{23b}$$

$$\dot{\varepsilon}_{z\theta} = 0. \tag{23c}$$

A Filon-based technique (Davis and Rabinowitz, 1984) is used to numerically evaluate the integrals in Eqs. (19a), (19b), and (21a)–(21c) for $|z/R| \leqslant \lambda = 0.1$. The stress–separation curves are then determined by evaluating the integrals in Eq. (6) by a Gauss–Legendre technique. The oscillating nature of the integrands in Eqs. (19) and (21) requires that attention be paid to convergence of the quadrature. The stress–separation curves computed using 16, 32, and 64 quadrature points are graphically indistinguishable. Thirty-two points were used to compute the results below.

The value of λ at which we switch from the eigenfunction expansion in Eq. (15) to the Fourier integral representation in Eq. (18) was determined by evaluating both representations for several combinations of ρ/R and z/R. Those calculations show that, when $|z/R| < 0.1$, a very large number of terms in Eq. (15) is required to achieve convergence. (In all the investigated cases, however, retention of a sufficiently large number of terms gave results that differed from the Fourier integral representation by less than 0.02%, even for $|z/R| = 10^{-3}$). Accordingly, we have used Eq. (15) for $|z/R| > \lambda = 0.1$, where it is rapidly convergent, and Eq. (18) for $|z/R| \leqslant \lambda = 0.1$.

Stress–separation curves are shown in Fig. 6, where the spacing between neighboring cavities is taken to be the same as the thickness of the adhesive layer ($H = R$). The abscissa measures the logarithmic strain at the cylinder ends, where d is the displacement at the cylinder ends. Trends similar to those in the spherically symmetric case are observed. However, the stress reaches its peak at a smaller strain (see the insert in Fig. 6).

Cavity shape evolution can be followed by calculating the displacement of each material point on the cavity boundary. Fig. 7 shows an example of cavity shape evolution for $R_0/R = 0.1$, $N = 0.1$, $\varepsilon_Y = 0.003$, and $H/R = 1$, where only the first quadrant is shown due to symmetry. We see that cavities remain essentially spherical up to radius $0.3R$, beyond which they become prolate because of a greater growth rate in the axial direction than in the radial direction. In reality, during the final stage of cavity evolution, the material between cavities necks down abruptly, and adjacent cavities coalesce. This necking process is not accounted for in our analysis. Therefore, near the end of the cavity growth process, the cavity shape and stress–separation curves predicted by our model may not be accurate.

5. Finite size effect for a nonhardening material

In the previous section, we studied cavity growth in a particular configuration under specific loading, namely, a cylindrical bar with a fixed cylinder wall subject to far-field tension at its ends. However, the model is not limited to such problems. Here we study

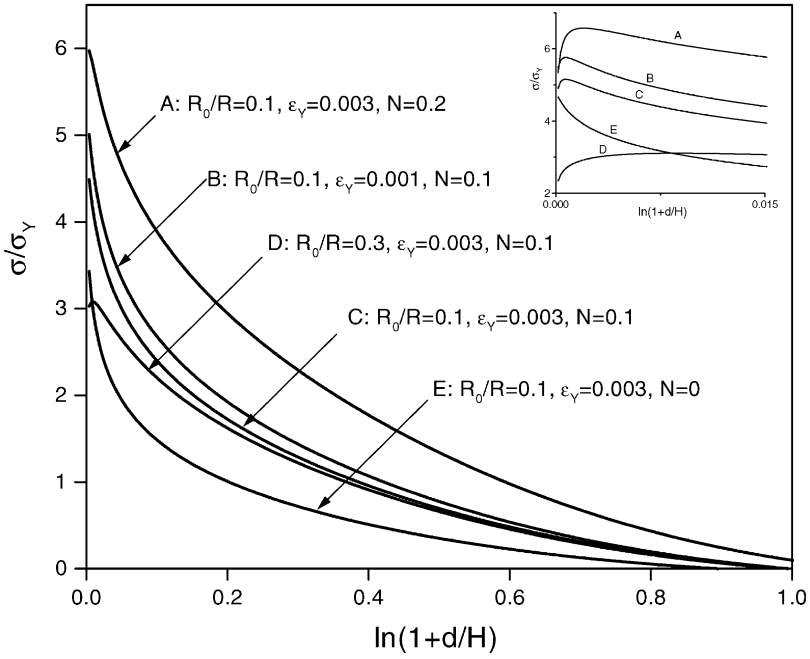

Fig. 6. Stress–separation relations for axisymmetric case ($H/R=1$).

cavity growth behavior under a more general loading of a finite body. The results can be compared with those of Rice and Tracey (1969) as the size of the body approaches infinity.

Consider again the cylindrical bar (Fig. 4) of an incompressible rigid–plastic material (nonhardening) subject to a general mean normal stress σ_m^B and deviatoric stress s_{ij}^B at the boundary. For a von Mises material following the $J-2$ flow rule, such traction boundary conditions will lead to a strain-rate field $\dot{\varepsilon}_{ij}^B$ at the boundary. To simplify the analysis, we choose a simple, volume-conservative strain-rate field at the boundary, consisting of extension at the rate $\dot{\varepsilon}^B$ in the z-direction and contraction at the rate $\dot{\varepsilon}^B/2$ in the ρ-direction, added to the cavitation field given in the previous section. We seek to determine the relation between the cavity expansion rate and the imposed mean normal stress and strain-rate field at the boundary. The assumed velocity field for the configuration consists of two parts: one associated with the potential ϕ, accounting mainly for the volume change of the cavity, and the other giving the strain-rate field $\dot{\varepsilon}_{ij}^B$ on the boundary, accounting for shape change of the cavity (Rice and Tracey, 1969). The velocity is then given by

$$\dot{u}_\rho = -\frac{1}{2}\rho\dot{\varepsilon}^B + \frac{\partial\phi}{\partial\rho}, \tag{24a}$$

$$\dot{u}_z = z\dot{\varepsilon}^B + \frac{\partial\phi}{\partial z}. \tag{24b}$$

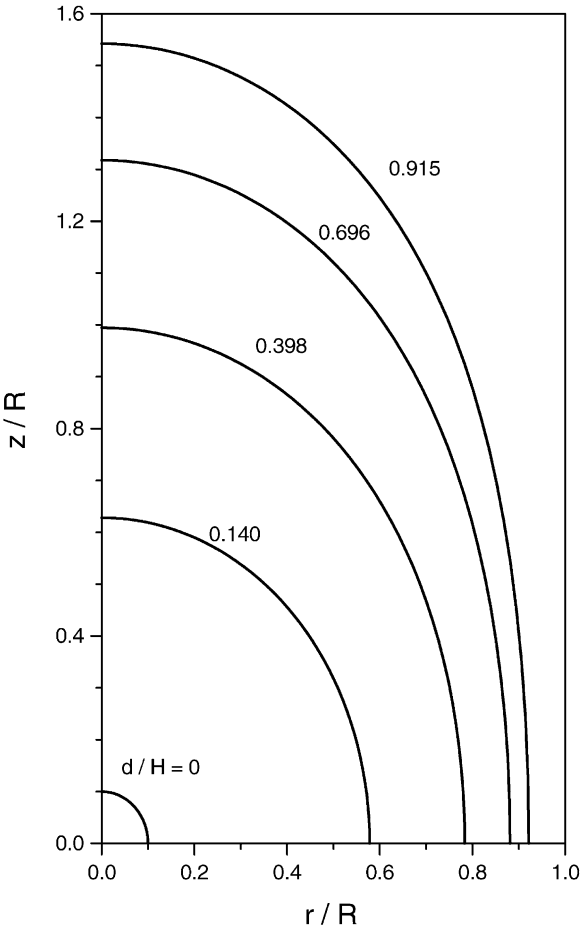

Fig. 7. Evolution of cavity shape for axisymmetric cavitation ($H/R = 1,\ R_0/R = 0.1$).

If the length of the cylindrical bar is at least twice its diameter, the contribution of the potential ϕ to the strain rates on the boundary is negligibly small, and the superposition of the two fields satisfies incompressibility and the boundary conditions. Using the principle of virtual work rate, a weak form of the equilibrium condition can be obtained (see Appendix B)

$$\int_V (s_{ij} - s^B_{ij})\dot{\varepsilon}^{\phi}_{ij}\,\mathrm{d}V = -\int_{S_V} n_i \sigma^B_{ij}\dot{u}^{\phi}_j\,\mathrm{d}S, \tag{25}$$

where S_V is the surface of the cavity, s^B_{ij} is the imposed deviatoric stress field at the boundary, and $\dot{u}^{\phi}_i$ and $\dot{\varepsilon}^{\phi}_{ij}$ are the velocity vector and strain-rate tensor associated with the potential, respectively. The cavity volume rate of change Q can then be expressed

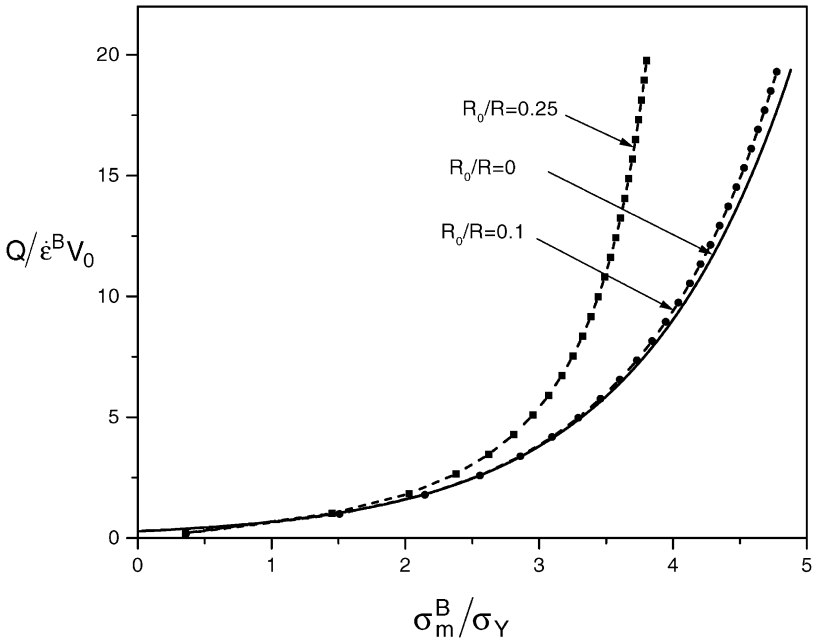

Fig. 8. Finite-body effect on cavity growth ($H/R = 2$).

as a function of hydrostatic stress σ_m^B and the tensile strain rate $\dot{\varepsilon}^B$ on the boundary as

$$Q = Q(R_0/R, \sigma_m^B/\sigma_Y, \dot{\varepsilon}^B) \ (H \geqslant 2R). \tag{26}$$

The cavity radius at any stage can be determined by integrating Eq. (26). As $R \to \infty$, the potential ϕ approaches that of a free point source and Q becomes independent of its first argument. In this limit, a closed-form solution

$$Q/(\dot{\varepsilon}^B V_0) = 0.283 \exp(3\sigma_m^B/2\sigma_Y) \ (H, R \to \infty), \tag{27}$$

was found by Rice and Tracey (1969), where $V_0 = 4\pi R_0^3/3$ is the initial cavity volume.

Fig. 8 shows the relationship between the dimensionless stress σ_m^B/σ_Y and normalized rate of change of cavity volume $Q/(\dot{\varepsilon}^B V_0)$. The solid line without symbols represents the limiting case (infinite body) given by Eq. (27). Our result using Eq. (26) approaches that of Rice and Tracey (1969) as $R_0/R \to 0$. Fig. 8 shows that if the imposed hydrostatic stress is less than twice the yield stress, the finite body effect is negligibly small. The effect is more profound at higher hydrostatic stresses. If the bar radius is 10 times the cavity radius, the difference between the finite-size and infinite-body results is very small up to $\sigma_m^B/\sigma_Y = 4$.

6. Fracture resistance

The analyses of the spherically symmetric and axisymmetric cases show that the stress–separation curves depend strongly on the hardening exponent and initial

cavity size, but weakly on the nominal strain ε_Y. A universal expression for the stress–separation curves can be written as

$$\sigma_s(d)/\sigma_Y = F(\Delta, N, V_f, G), \tag{28}$$

where N is the hardening exponent, $\Delta(=d/H)$ is the normalized end displacement, V_f is the cavity density in the interfacial layer, directly related to the interfacial surface microstructure, and G is a geometric parameter related to the thickness of the ductile layer and the spacing between neighboring cavities. For the cylindrical bar case, we take $V_f = R_0/R$ and $G = H/R$, and identify G as an aspect ratio.

As pointed out by Tvergaard and Hutchinson (1992, 1996), two important factors characterizing the stress–separation curves are the work of separation per unit area (the initial separation resistance), Γ_0, and the peak stress. The latter can be readily determined from the stress–separation curves obtained in the previous sections. The initial separation resistance can be evaluated by integrating the corresponding stress–separation curves

$$\Gamma_0 = W/A = \frac{2}{\pi R^2}\int_0^{U_I^*} T_s(U_I)\,\mathrm{d}U_I, \tag{29}$$

where W is the work of separation for the cylindrical bar, $A = \pi R^2$ is the exposed area, U_I^* the displacement at which total separation occurs ($\sigma_s \approx 0$), and T_s is the resultant traction at the ends of the cylindrical bar. To facilitate the calculation, a normalized initial fracture resistance Γ_0 can be written as

$$\frac{\Gamma_0}{2R\sigma_Y} = G\int_0^{\varepsilon^*} [\sigma_s(\varepsilon)/\sigma_Y]\mathrm{e}^{\varepsilon}\,\mathrm{d}\varepsilon, \tag{30}$$

where ε^* is the true average strain corresponding to the end displacement U_I^* evaluated at the ends of the cylindrical bar.

Eq. (30) shows that the normalized initial fracture resistance is determined solely by the stress–separation curves. Since the stress–separation curves are nearly independent of the nominal strain, so is the normalized initial fracture resistance. The dependence of the normalized initial fracture resistance on geometry is shown in Fig. 9(a). The dashed line in Fig. 9(a) shows the maximum value of the normalized fracture resistance as $H/R \to \infty$. For a given strain-hardening exponent and initial cavity density, the normalized fracture resistance increases monotonically and approaches its maximum value asymptotically as the aspect ratio increases. For $H/R > 4.0$, the normalized fracture resistance does not change significantly (less than 2%) and is nearly independent of H/R. For $H/R < 1.0$, nonuniformity of the velocity field at the cylinder ends renders the results of our approach inaccurate. Fig. 9(b) shows that the normalized initial fracture resistance increases considerably as the strain-hardening exponent increases. Over the range $0 \leqslant N \leqslant 0.3$, our model predicts a more than fourfold variation of the normalized initial fracture resistance. Fig. 9(c) shows that Γ_0 decreases slightly as V_f increases, indicating that the effect of initial cavity size on the peak stress of the stress–separation curves is more significant than its effect on the interfacial fracture resistance.

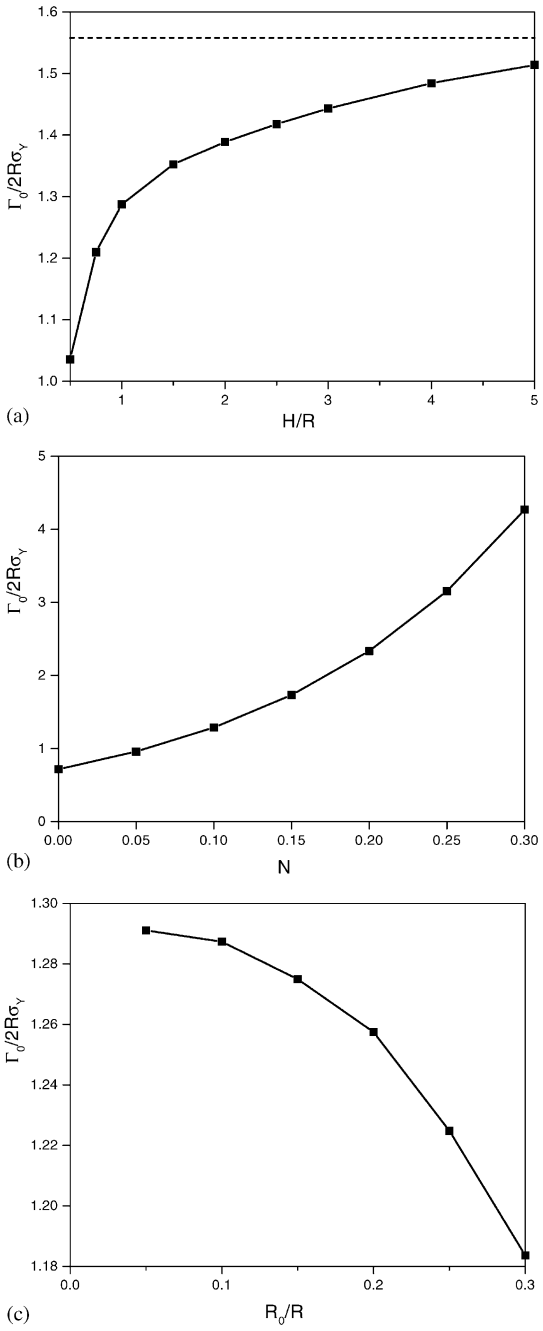

Fig. 9. (a) Normalized initial fracture resistance versus the aspect ratio H/R ($R_0/R = 0.1$, $N = 0.1$). (b) Normalized initial fracture resistance versus the strain-hardening exponent N ($H/R = 1$, $R_0/R = 0.1$). (c) Normalized initial fracture resistance versus initial cavity density R_0/R ($H/R = 1$, $N = 0.1$).

7. Discussion

We have addressed a particular mechanism of interfacial fracture—cavitation in a thin, ductile layer in a sandwich structure. A new technique has been developed to solve cavitation problems involving large plastic deformation, for which closed-form solutions of the full elastic–plastic deformation problem are not obtainable. For a rigid–plastic material, our technique approximates the plastic deformation field by a potential flow field, which can be determined as the solution of an elliptic boundary-value problem. Full stress–separation relations are then obtained by applying the principle of virtual work rate. The two important factors for interfacial fracture, initial fracture resistance and peak stress, can be extracted directly from the stress–separation curves or obtained by integrating the stress–separation curves.

Two configurations have been considered in this paper: a cavity centered in a sphere, for which a closed-form solution exists; and a cavity centered in a circular cylinder, for which no closed-form solution is available. For each case, a flow field associated with a point source and satisfying prescribed boundary conditions is used to approximate the complex plastic deformation field around the cavity. The method uses the principle of virtual work rate to approximately (but not pointwise) satisfy the equilibrium conditions, and does not account for elastic deformation. For cavity growth in a sphere, this technique gives the exact solution. For the cylindrical bar, reliable stress–separation curves have been obtained by this technique. The stress–separation relation is shown to depend strongly on the strain-hardening exponent and initial cavity size, and weakly on the nominal strain.

Under load-controlled loading, cavity growth in an elastic–plastic solid reaches instability (i.e., infinite growth rate) at a critical stress level (Huang et al., 1991). On the other hand, under displacement-controlled loading, the stress versus cavity growth curve for an elastic–plastic material goes through stages where the stress increases, reaches a peak stress, and then decreases, ultimately to zero, as the cavity grows. Under displacement-controlled loading, the level of the peak stress corresponds to the critical stress for cavitation instability under load-controlled loading. Huang et al. (1991) showed that, for an elastic–perfectly plastic solid, such instability exists under load-controlled loading only if elastic deformation is included. In our model, a rigid–plastic (nonhardening or hardening) constitutive law is used, and no account is taken of elasticity. However, the insert in Fig. 6 shows that, for hardening materials ($N > 0$), the stress increases before reaching the peak stress and then decreases; whereas for a perfectly plastic material ($N = 0$), the stress–separation curve decreases monotonically from the beginning. Similar results were obtained by Zhang and Hsia (2001) for plane-strain cavity growth in rigid–plastic materials. These results indicate that, for load-controlled loading, cavitation instability will occur for plastic hardening materials, even if elastic deformation is excluded.

Parametric study of the initial fracture resistance provides guidance to the development of processes for surface preparation of adherends for bonded joints. For a given interfacial microstructure, the results in Fig. 9(b) show that increasing the hardening exponent can considerably improve interfacial fracture toughness. However, interfacial layer thickness has only a limited effect on interfacial fracture resistance as long

as the thickness is comparable to the spacing between adjacent cavities, as shown in Fig. 9(a). Fig. 9(c) shows that the fracture resistance decreases monotonically with increasing initial cavity volume fraction, indicating that an interfacial microstructure with sparsely distributed cavity nucleation sites is preferable. On the other hand, surface preparation processes that give rise to smaller initial cavity size are desirable since a higher peak stress is needed for interfacial crack propagation, as shown in Fig. 6. It is therefore crucial to develop surface preparation processes that minimize formation of large cavities, which can significantly degrade interface performance.

For the cylindrical bar, Fig. 10 shows the stress–separation curves predicted by the current model and that of Tvergaard (1997). The aspect ratio H/R, initial cavity size R_0, and strain-hardening exponent N used in the current calculation are identical to those in Tvergaard's work. Although the results agree well at low values of the normalized end displacement d/H, there is significant divergence at higher d/H.

The main differences between our work and Tvergaard's are as follows. The approach of Tvergaard approximates the displacement field with a discrete, kinematically admissible field and enforces the equilibrium condition using variational principles, whereas our approach approximates the displacement field with a continuum, potential flow solution and enforces equilibrium by the principle of virtual work rate. Tvergaard's solution satisfies all solid mechanics governing equations and should, in principle, converge to the true solution as the finite-element mesh is refined. Our solution for the deformation field, on the other hand, satisfies the potential flow governing equation and can only be treated as an approximation to the real plastic deformation field. Another difference is that elasticity is not accounted for in our analysis. Moreover, Tvergaard's approach requires repeated remeshing at large deformations, whereas our method deals with arbitrarily large deformation in a unified way.

Inaccurate approximation of plastic deformation by potential flow may be the principal cause of the discrepancies shown in Fig. 10. As depicted in Fig. 7, the potential-flow solution predicts that a cavity grows more rapidly normal to the interface than parallel to it, while finite-element analysis of the solid mechanics governing equations predicts that parallel growth is more rapid than perpendicular growth (Tvergaard, 1997). Thus, for a regular array of cavities with equidistantly spaced centers and equal volumes, our model predicts that more load-bearing material remains between adjacent cavities than does the finite-element analysis. This leads to a correspondingly higher prediction of the separation stress.

Our results show that, for the infinite body case, our approach has the same degree of accuracy as that of Rice and Tracey (1969). It was pointed out by Huang (1991) that, since the perturbation-based Rice and Tracey solution does not use a complete set of functions to represent the deformation field, it underestimates the cavity growth rate. A consequence of this underestimation is that the material is predicted to be stiffer than it really is. This is consistent with the discrepancies between our results and those of Tvergaard (1997).

In this paper, periodic interaction between adjacent cavities is modeled by specifying Neumann boundary conditions for a single cell. While unstable coalescence of adjacent cavities will cause the separation stress to drop to zero rapidly, the current method does

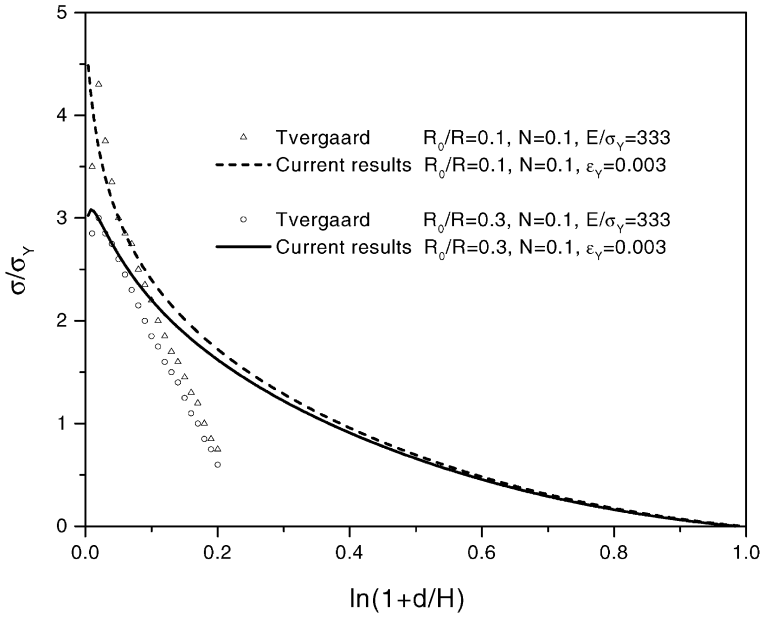

Fig. 10. Comparison of the present results to those of Tvergaard (1997) ($H/R = 1$).

not take this necking process into account. This final stage of the separation process, however, contributes insignificantly to the overall fracture resistance.

The current paper makes use of a feature common to the rigid–plastic deformation field in solid mechanics and the potential flow in fluid mechanics, namely incompressibility. The present work suggests that the current approach can be applied to a variety of solid mechanics problems, provided that elastic deformation is negligible. Compared to the computational burden of the finite-element method and remeshing at each stage, this method has clear advantages for detailed parametric studies.

Acknowledgements

This material is based upon work supported by the U.S. Department of Energy, Division of Materials Sciences under Grant DEFG02-96ER45607, through the Frederick Seitz Materials Research Laboratory at the University of Illinois at Urbana-Champaign.

Appendix A.

More generally, Eqs. (13) and (14a) can be written as

$$\nabla^2\psi(\boldsymbol{x},\boldsymbol{x}') = Q\delta(\boldsymbol{x}-\boldsymbol{x}') = \frac{Q}{2\pi\rho}\delta(\rho-\rho')\delta(z-z'), \tag{A.1}$$

and

$$\frac{\partial\psi(\boldsymbol{x},\boldsymbol{x}')}{\partial\rho}=0 \quad \text{at } \rho=R, \tag{A.2}$$

where $\boldsymbol{x}=(\rho,z)$ and $\boldsymbol{x}'=(\rho',z')$ represent axisymmetric cylindrical coordinates and the singularity location, respectively.

It should be noted that ψ is essentially a Green's function satisfying a Neumann boundary condition on the cylinder wall. Thus, it is symmetric with respect to $\boldsymbol{x}$ and $\boldsymbol{x}'$. The delta function in Eq. (A.1) can be written as

$$\delta(z-z')=\frac{1}{2\pi}\int_{-\infty}^{\infty}\mathrm{e}^{ik(z-z')}\,\mathrm{d}k=\frac{1}{\pi}\int_{0}^{\infty}\cos k(z-z')\,\mathrm{d}k, \tag{A.3}$$

It is convenient to express the potential as a product of functions appropriate to cylindrical coordinates, in a similar fashion as Eq. (A.3)

$$\psi(\boldsymbol{x},\boldsymbol{x}')=\frac{Q}{2\pi^2}g(\rho,\rho')\int_{0}^{\infty}\cos k(z-z')\,\mathrm{d}k, \tag{A.4}$$

where g satisfies

$$\frac{1}{\rho}\frac{\mathrm{d}}{\mathrm{d}\rho}\left[\rho\frac{\mathrm{d}g}{\mathrm{d}\rho}\right]-k^2g=\frac{1}{\rho}\delta(\rho-\rho'). \tag{A.5}$$

When $\rho\neq\rho'$, the solution of Eq. (A.5) is a linear combination of zeroth-order modified Bessel functions

$$g(\rho,\rho')=\begin{cases} AI_0(k\rho)+CK_0(k\rho), & (\rho<\rho'),\\ BI_0(k\rho)+DK_0(k\rho), & (\rho>\rho') \end{cases} \tag{A.6}$$

where A, B, C, and D are coefficients to be determined. For $\rho\neq\rho'$, g is bounded, hence $C=0$. The Neumann condition at the cylinder wall leads to $D=BI_1(kR)/K_1(kR)$, where I_1 and K_1 are the first-order modified Bessel functions. Substituting this into Eq. (A.6) gives

$$g(\rho,\rho')=\begin{cases} AI_0(k\rho), & (\rho<\rho'),\\ B\left[I_0(k\rho)+\dfrac{I_1(kR)}{K_1(kR)}K_0(k\rho)\right], & (\rho>\rho'). \end{cases} \tag{A.7}$$

Using the symmetry of the potential ψ in ρ and ρ', one has

$$g(\rho,\rho')=\mu I_0(k\rho_{\min})\left[I_0(k\rho_{\max})+\frac{I_1(kR)}{K_1(kR)}K_0(k\rho_{\max})\right], \tag{A.8}$$

where

$$\rho_{\min}=\min(\rho,\rho'), \tag{A.9a}$$
$$\rho_{\max}=\max(\rho,\rho') \tag{A.9b}$$

and $\mu=AB$. The discontinuity in the slope of g implied by Eq. (A.5) gives

$$\lim_{\Delta\rho\to0}\left[\left.\frac{\mathrm{d}g}{\mathrm{d}\rho}\right|_{\rho'+\Delta\rho}-\left.\frac{\mathrm{d}g}{\mathrm{d}\rho}\right|_{\rho'-\Delta\rho}\right]=\frac{1}{\rho'}. \tag{A.10}$$

Substituting Eq. (A.8) into Eq. (A.10), one has

$$\mu = -\frac{K_1(kR)}{I_1(kR)}. \tag{A.11}$$

Thus, the potential can be rewritten as

$$\psi(\boldsymbol{x},\boldsymbol{x}') = -\frac{Q}{2\pi^2}\int_0^\infty \cos k(z-z')I_0(k\rho_{\min}) \times \left[\frac{K_1(kR)}{I_1(kR)}I_0(k\rho_{\max}) + K_0(k\rho_{\max})\right] \mathrm{d}k. \tag{A.12}$$

For $\rho' = 0$, $\rho_{\min} = 0$ and $\rho_{\max} = \rho$, we have

$$\psi(\boldsymbol{x}) = -\frac{Q}{2\pi^2}\int_0^\infty \cos k(z-z')\left[\frac{K_1(kR)}{I_1(kR)}I_0(k\rho) + K_0(k\rho)\right] \mathrm{d}k. \tag{A.13}$$

Appendix B

For the assumed velocity field in Eqs. (24a) and (24b), the principle of virtual work rate in Eq. (3) can be rewritten as

$$\int_S n_i\sigma_{ij}(\dot{u}_j^B + Q\dot{u}_j^\phi)\,\mathrm{d}S = \int_V \sigma_{ij}(\dot{\varepsilon}_{ij}^B + Q\dot{\varepsilon}_{ij}^\phi)\,\mathrm{d}V, \tag{B.1}$$

where $\dot{u}_i^B$ and $\dot{\varepsilon}_{ij}^B$ are the displacement-rate and strain-rate fields, respectively, corresponding to the first terms on the right-hand sides of Eqs. (24a) and (24b). According to Gauss' divergence theorem, one has

$$\int_S n_i\sigma_{ij}\dot{u}_j^B\,\mathrm{d}S = \int_V \sigma_{ij}\dot{\varepsilon}_{ij}^B\,\mathrm{d}V. \tag{B.2}$$

Subtracting Eq. (B.2) from (B.1), one has

$$\int_S n_i\sigma_{ij}\dot{u}_j^\phi\,\mathrm{d}S = \int_V \sigma_{ij}\dot{\varepsilon}_{ij}^\phi\,\mathrm{d}V. \tag{B.3}$$

Based on the traction-free condition on the cavity surface, the surface integral in Eq. (B.3) can be rewritten as

$$\int_S n_i\sigma_{ij}\dot{u}_j^\phi\mathrm{d}S = \int_{S_\infty} n_i\sigma_{ij}^B\dot{u}_j^\phi\,\mathrm{d}S = \int_S n_i\sigma_{ij}^B\dot{u}_j^\phi\,\mathrm{d}S - \int_{S_V} n_i\sigma_{ij}^B\dot{u}_j^\phi\,\mathrm{d}S, \tag{B.4}$$

where S_∞ and S_V are the boundaries at infinity and on the cavity surface, respectively. Applying Gauss' divergence theorem to the first term on the right-hand side of Eq. (B.4), one obtains

$$\int_V \sigma_{ij}\dot{\varepsilon}_{ij}^\phi\,\mathrm{d}V = \int_V \sigma_{ij}^B\dot{\varepsilon}_{ij}^\phi\,\mathrm{d}V - \int_{S_V} n_i\sigma_{ij}^B\dot{u}_j^\phi\,\mathrm{d}S. \tag{B.5}$$

Note that $\dot{\varepsilon}_{ii}^\phi = 0$ according to the incompressibility condition, from which one obtains Eq. (25).

References

Ashby, M.F., Blunt, F.J., Bannister, M., 1989. Flow characteristics of highly constrained metal wires. Acta Metall. 37, 1847–1857.

Berg, P.W., McGregor, J.L., 1966. Elementary Partial Differential Equations. Holden-Day, San Francisco.

Clearfield, H.M., McNamara, D.K., Davis, G.D., 1990. ASM Engineered Materials Handbook, Vol. 3, Metals Park, OH, pp. 259–275.

Davis, P.J., Rabinowitz, P., 1984. Methods of Numerical Integration, 2nd Edition. Academic Press, Orlando.

Evans, A.G., Dalgleish, B.J., 1992. The fracture resistance of metal–ceramic interfaces. Acta Metall. Mater. 40, S295–S306.

Gao, H., Scheeline, A., Pearlstein, A.J., 1999. Demonstration of a novel rotating cylindrical electrode in growth of oxide films with spatially controlled microstructural variation on Al 6061. In: Leddy, J., Vanysek, P., Porter, M.D. (Eds.), Proceedings of the International Symposium on New Directions in Electroanalytical Chemistry, II, 1999. The Electrochemical Society, Pennington, NJ, pp. 116–124.

Hou, H.-S., Abeyaratne, R., 1992. Cavitation in elastic and elastic–plastic solids. J. Mech. Phys. Solids 40, 571–592.

Huang, Y., 1991. Accurate dilatation rates for spherical voids in triaxial stress fields. J. Appl. Mech. 58, 1084–1086.

Huang, Y., Hutchinson, J.W., Tvergaard, V., 1991. Cavitation instabilities in elastic–plastic solids. J. Mech. Phys. Solids 39, 223–241.

Lamb, H., 1932. Hydrodynamics, 6th Edition. Cambridge University Press, New York.

Mao, S.X., Evans, A.G., 1997. The influence of blunting on crack growth at oxide/metal interfaces. Acta Mater. 45, 4263–4270.

McMeeking, R.M., Rice, J.R., 1975. Finite-element formulations for problems of large elastic–plastic deformation. Int. J. Solids Struct. 11, 601–616.

Rice, J.R., Tracey, D.M., 1969. On the ductile enlargement of voids in triaxial stress fields. J. Mech. Phys. Solids 17, 201–217.

Tvergaard, V., 1997. Studies of void growth in a thin ductile layer between ceramics. Comput. Mech. 20, 186–191.

Tvergaard, V., Hutchinson, J.W., 1992. The relation between crack growth resistance and fracture process parameters in elastic–plastic solids. J. Mech. Phys. Solids 40, 1377–1397.

Tvergaard, V., Hutchinson, J.W., 1993. Effect of initial void shape on the occurrence of cavitation instabilities in elastic–plastic solids. J. Appl. Mech. 60, 807–812.

Tvergaard, V., Hutchinson, J.W., 1996. Effect of strain-dependent cohesive zone model on predictions of crack growth resistance. Int. J. Solids Struct. 33, 3297–3308.

Zhang, S., Hsia, K.J., 2001. Modeling the fracture of a sandwich structure due to cavitation in a ductile adhesive layer. J. Appl. Mech. 68, 93–100.